Chemically Derived, Ultrasmooth Graphene Nanoribbon Semiconductors

Xiaolin Li, *et al.*

Science **319**, 1229 (2008);
DOI: 10.1126/science.1150878

18. D. A. Bonn, *Nat. Phys.* **2**, 159 (2006).
19. S. Ilani, A. Yacoby, D. Mahalu, H. Shtrikman, *Science* **292**, 1354 (2001).
20. J. Feist *et al.*, *Phys. Rev. Lett.* **97**, 116804 (2006).
21. We thank the team of the Ben-Gurion University Weiss Family Laboratory for Nanoscale Systems for the fabrication of the chip, and J. Jopp of the Ben-Gurion University Ilse Katz Center for Nanoscale Science for assisting with surface measurements. R.F. thanks Y. Imry and A. Klug for their continued support. Supported by the Fonds zur Förderung der Wissenschaftlichen Forschung, Deutsche Forschungsgemeinschaft, German Federal Ministry of Education and Research (Deutsch-Israelische Projektkooperation), European Community "Atomchip" Research Training Network, American-Israeli Binational Science Foundation, and Israeli Science Foundation.

Supporting Online Material
www.sciencemag.org/cgi/content/full/319/5867/1226/DC1
Materials and Methods
Figs. S1 to S3
References

1 November 2007; accepted 7 January 2008
10.1126/science.1152458

Chemically Derived, Ultrasmooth Graphene Nanoribbon Semiconductors

Xiaolin Li,* Xinran Wang,* Li Zhang, Sangwon Lee, Hongjie Dai†

We developed a chemical route to produce graphene nanoribbons (GNR) with width below 10 nanometers, as well as single ribbons with varying widths along their lengths or containing lattice-defined graphene junctions for potential molecular electronics. The GNRs were solution-phase–derived, stably suspended in solvents with noncovalent polymer functionalization, and exhibited ultrasmooth edges with possibly well-defined zigzag or armchair-edge structures. Electrical transport experiments showed that, unlike single-walled carbon nanotubes, all of the sub–10-nanometer GNRs produced were semiconductors and afforded graphene field effect transistors with on-off ratios of about 10^7 at room temperature.

Graphene (single-layer graphite) has emerged as a material with interesting low-dimensional physics and potential applications in electronics (*1*–*6*). Graphene nanoribbons (GNRs), if made into quasi-one-dimensional structures with narrow widths (<~10 nm) and atomically smooth edges, are predicted to exhibit band gaps useful for room-temperature transistor operations with excellent switching speed and high carrier mobility (potentially even ballistic transport) (*7*–*13*). Recent theoretical work predicted that quantum confinement and edge effects make narrow GNRs (width w < ~10 nm) into semiconductors, which differs from single-walled carbon nanotubes (SWNTs) that contain ~1/3 metallic species.

Lithographic patterning of graphene sheets has fabricated GNRs down to widths of ~20 nm thus far (*12*, *13*), but there are difficulties in obtaining smooth edges (for example, with roughness < ~5 nm) and reaching true nanometer-scale ribbon width. Chemical approaches (*14*–*17*) and self-assembly processes may produce graphene structures with desired shape and dimensions for fundamental and practical applications.

We report that, by using a widely available and abundant graphite material, we can develop simple chemical methods to produce GNRs. We exfoliated commercial expandable graphite (Grafguard 160-50N, Graftech Incorporated, Cleveland, OH) by brief (60 s) heating to 1000°C in forming gas (3% hydrogen in argon). The resulting exfoliated graphite was dispersed in a 1,2-dichloroethane (DCE) solution of poly(m-phenylenevinylene-co-2,5-dioctoxy-p-phenylenevinylene) (PmPV) by sonication for 30 min to form a homogeneous suspension. Centrifugation then removed large pieces of materials from the supernatant (Fig. 1A and fig. S1) (*18*).

We used atomic force microscopy (AFM) to characterize the materials deposited on substrates from the supernatant and observed numerous GNRs with various widths ranging from w ~ 50 nm down to sub-10 nm (Fig. 1, B to F). Topographic heights of the GNRs (average length ~ 1 μm) were mostly between 1 and 1.8 nm, which correspond to a single layer (e.g., Fig. 1B, left image) or a few layers (mostly ≤3 layers). Smooth edges were observed for the GNRs, with edge roughness well below ribbon width even for $w \leq 10$ nm. Accurate measurements of GNR width were difficult because of the finite AFM tip radius (~10 to 20 nm), especially for ultranarrow ribbons. To circumvent the problem, we used the same tips to measure the apparent widths of Hipco (Carbon Nanotechnologies Incorporated, Houston, TX)

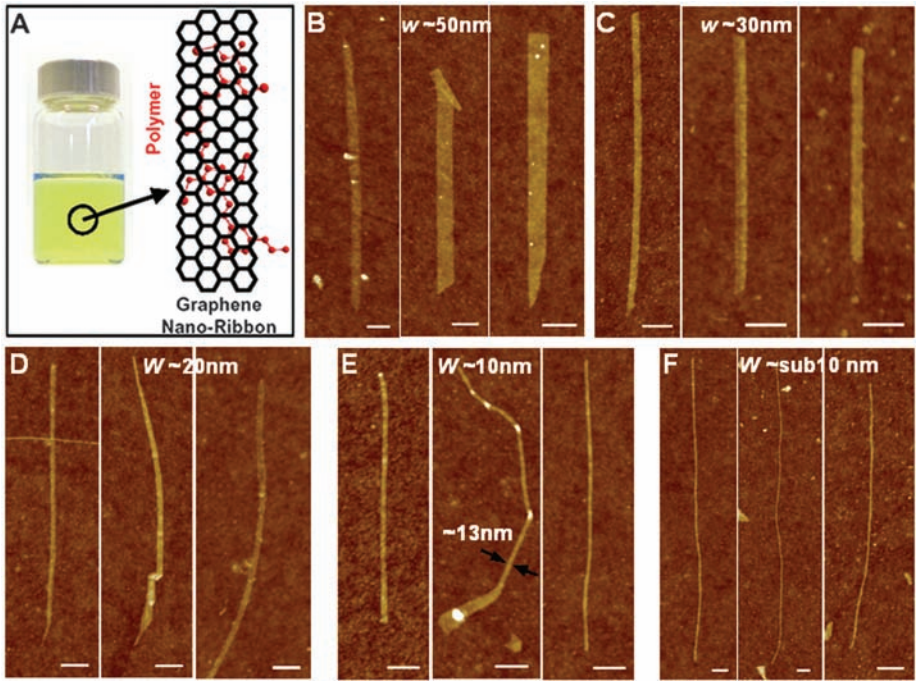

Fig. 1. Chemically derived graphene nanoribbons down to sub-10-nm width. (**A**) (Left) Photograph of a polymer PmPV/DCE solution with GNRs stably suspended in the solution. (Right) Schematic drawing of a graphene nanoribbon with two units of a PmPV polymer chain adsorbed on top of the graphene via π stacking. (**B** to **F**) AFM images of selected GNRs with widths in the 50-nm, 30-nm, 20-nm, 10 nm and sub-10-nm regions, respectively. A substrate (300-nm-thick $SiO_2/p^{++}Si$) was soaked in a GNR suspension for 20 min for deposition, rinsed, blow-dried, and calcined at 400°C to remove PmPV before AFM. Some of the GNRs narrow down to a sharp point near the ends. In (B), left ribbon height ~ 1.0 nm, one layer; middle ribbon height ~ 1.5 nm, two layers; right ribbon height ~ 1.5 nm, two layers. In (C), the three GNRs are two to three layers thick. In (D), ribbons are one (right image) to three layers. Two GNRs crossing in the left image are observed. In (E), ribbons are two- to three-layered. In the middle image, a single ribbon exhibits varying width along its length with mechanical bends (bright regions) between segments. In (F), the heights of the ultranarrow ribbons are ~1.5, 1.4, and 1.5 nm, respectively. All scale bars indicate 100 nm.

Department of Chemistry and Laboratory for Advanced Materials, Stanford University, Stanford, CA 94305, USA.

*These authors contributed equally to this work.
†To whom correspondence should be addressed. E-mail: hdai@stanford.edu

SWNTs in a diameter-separated sample and deduced tip size (*18*). All GNR widths reported in this work have their basis in AFM measurements after correcting for the tip-size effect.

Transmission electron microscopy (TEM, fig. S5) (*18*), electron diffraction (fig. S5) (*18*), and Raman spectroscopy (fig. S6) (*18*) (graphene G-band) were used to characterize the GNRs. Because of their topographical resemblance to SWNTs, we carried out extensive control experiments to ensure that the sub-10-nm GNRs in our samples were not SWNTs present from contamination or other causes. For example, we performed surface-enhanced Raman measurements on many GNR samples deposited on Au substrates and never observed any radial breathing modes intrinsic to SWNTs (fig. S6) (*18*). Further, all of our $w < 10$ nm GNRs were semiconductors (see below), unlike SWNTs, which form as mixtures in which one-third of nanotubes are metallic.

The formation of our GNRs constitutes several key steps. First, ~350-μm-scale graphite flakes were made into expandable graphite by chemical intercalation of oxidizing sulfuric acid and nitric acid, with oxidation of carbon atoms likely occurring at the edge, step, and defect sites of graphite (*19*, *20*). Second, rapid heating of the expandable graphite to 1000°C caused violent formation of volatile gaseous species from the intercalant and exfoliates graphite into a loose stack of few-layered graphene sheets. This thermal exfoliation step is critical and responsible for the formation of one- to few-layer graphene and was evidenced by a visible, dramatic volume expansion of graphite by ~100 to 200 times after exfoliation (fig. S1) (*18*). The 1000°C treatment can also reverse oxidation and functionalization of graphite by thermally desorbing covalently attached species and repair defects (*21*).

Solution-phase sonication and functionalization by PmPV of few-layered graphene sheets formed by 1000°C exfoliation led to stably suspending graphene in DCE. The PmPV conjugated polymers (Fig. 1A), known to adsorb onto SWNT sidewalls via π stacking, noncovalently functionalized the exfoliated graphene to afford a homogeneous black suspension during sonication (fig. S1) (*18*, *22*, *23*). We were not able to form homogeneous suspension by the same process without using PmPV. We suggest that sonication is responsible for chemomechanical breaking of the stably suspended graphene sheets into smaller pieces, including nanoribbons. Sonochemistry and ultrahot gas bubbles involved in sonication cause graphene to break into various structures, with an appreciable yield of GNRs. The supernatant after centrifugation contains micrometer-sized graphene sheets and GNRs (albeit at lower yield than sheets) in various sizes, shapes, and morphologies.

Besides regularly shaped ribbons, we observed graphene structures that were shaped irregularly, such as wedges (Fig. 2), GNRs with bends and kinks (Fig. 2, A, B, and E), and ribbons coming off larger pieces of graphene with varying widths along the ribbon length [Fig. 1E, middle image, and fig. S5, TEM data (*18*)]. These results suggest that GNRs could be formed by breaking off narrow pieces of graphene from larger sheets during sonication. However, we found that continuous sonication does not lead to higher yield of GNRs and that the degree of sonication needs to be controlled for optimal yield of GNRs. Imaging with AFM indicated that almost no sub-10-nm ribbons were obtained if sonication were excessive (for hours) because of continued cutting and breaking of ribbons into small particle-like structures.

The observed graphene nanoribbons narrowing down to diminishing width and to a point (Fig. 2, C and D) indicate that GNRs reaching true nanometer dimensions with potentially atomic-scale smoothness can form. GNRs comprised of segments of varying widths (Fig. 1E, middle image, and 2B) could be used for graphene molecular electronics with varying band gaps along the ribbon. Interestingly, GNR junctions with sharp kinks at 120° angle were observed (Fig. 2B), apparently through the joining of two GNRs with edges along well-defined atomic lattice of graphene (such as zigzag edges). Single-layered GNRs displayed remarkably mechanical flexibility and resilience, with mechanical bending and folding without obvious breakage (Fig. 2E).

Next, we fabricated field-effect transistor (FET)–like devices with our GNRs (w ~ sub-10 nm to ~55 nm). The devices had palladium (Pd) as source/drain (S/D) metal contacts (channel length L ~ 200 nm), a p^{++}-Si backgate, and 300-nm SiO_2 as gate dielectrics (*18*). We observed that the room-temperature on-off current switching (I_{on}/I_{off}) induced by the gate voltage increased exponentially as the GNR width decreased, with I_{on}/I_{off} ~1, ~5, ~100, and $>10^5$ for w ~ 50 nm [fig. S7 (*18*)], w ~ 20 nm [fig. S7 (*18*)], w ~ 10 nm (Fig. 3A), and w ~ sub-10-nm (Fig. 3C) GNRs, respectively. This trend was consistent with lithographically fabricated GNRs with $w > 20$ nm (*12*). Importantly, all of the w = sub-10-nm GNRs characterized in our experiments (more than 30, with no exceptions) exhibited $I_{on}/I_{off} > 10^5$ (Fig. 4A) even under a S/D bias V_{ds} up to ~1 V. This suggests that the GNRs are semiconducting and have substantial band gaps. This result is in stark contrast to SWNTs (with circumference ~ sub-10 nm, or diameter < ~3 nm) that contain 1/3 metallic species. Thus, our chemically derived GNRs afford graphene transistors with orders of magnitude on/off switching at room temperature.

We could estimate the band gaps (E_g) of our GNRs by $I_{on}/I_{off} \propto \exp(E_g/k_BT)$ (where k_B is the Boltzmann's constant and T is temperature) in our p-type uni-polar GNR FETs because the off current of the device was thermally activated through a body-Schottky barrier (SB) to the conduction band on the order of ~E_g [the SB to holes in our GNR FETs was small, as is the case for Pd-contacted SWNT FETs, because of the high work function of Pd (*24*)]. The band gaps extracted this way were fit into an empirical form of $E_g(\text{eV}) = \frac{0.8}{W(\text{nm})}$ (Fig. 4B), which was con-

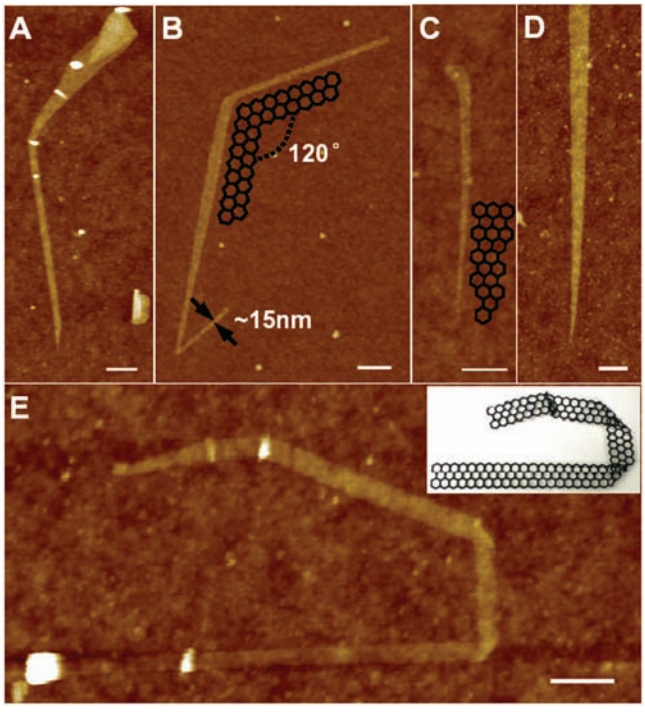

Fig. 2. Graphene nanoribbons with interesting morphologies and graphene-junctions. (**A** and **B**) AFM images of GNRs with junctions formed by different graphene structures at the two sides of the junctions. In (A), a w ~ 25 nm ribbon (two layers) forming a junction with a wedgelike graphene. In (B), a single-layer (height ~ 1.0 nm) graphene structure with three graphene segments of different widths forming two junctions. The well-defined 120° angle of the top junction suggests that the graphene segments near the kink likely have zigzag edges, as shown in the schematic drawing of the inset. (**C** and **D**) AFM images of knifelike graphene ribbons with width changing narrowing down from tens of nanometers to ultra sharp points. In (C), the ribbon is monolayer graphene with height ~ 1.0 nm. Inset of (C) A schematic drawing to illustrate the sharp tip. In (D), the ribbon is three-layer graphene with height ~ 1.9 nm. (**E**) AFM image of a GNR with several bends and folds involving mechanical deformations. It is a monolayer graphene ribbon with height ~ 1.1 nm. Inset of (E) A schematic drawing of the ribbon. All scale bars are 100 nm.

sistent with the exponential increase in I_{on}/I_{off} of our GNR FETs as ribbon width decreased. Possible errors in our E_g versus w analysis include uncertainties in w based on AFM and in the assumption of negligible SB for holes in ultranarrow (e.g., w < ~3 nm) GNR FETs.

First-principles calculations have suggested that GNRs open up band gaps through quantum confinement and edge effects and that $E_g \sim 1/w^{\alpha}$, where α is near unity (*7*, *8*). In armchair-edged GNRs, band gaps arise from quantum confinement and increased hopping integral of the π orbitals of the edge atoms caused by slight changes in atomic bonding lengths. In zigzag-edged GNRs, band gaps result from a staggered sublattice potential from magnetic ordering (*7*). The all-semiconductor nature found for our sub-10-nm GNRs is consistent with the band gap opening in GNRs with various edge structures suggested theoretically (*7*, *8*). Band gap values extracted from our experimental data fall in between the limits of theoretical calculations (*7*) for zigzag- and armchair-edged GNRs with various widths (Fig. 4B). More quantitative comparisons of our extracted band gaps with theory are difficult at the present time because the precise edge structures of the GNRs in our FETs are unknown and are likely to vary between ribbons in various devices with either zigzag, armchair, or mixed edges.

Our $w \sim$ sub-10-nm GNR devices deliver up to ~200 μA/μm on-current at $V_{ds} = 0.5$ V for $L \sim 200$ to 300 nm ribbon channel length, which is lower than the projected performance (~1000 μA/μm) for ballistic GNR transistors with similar widths (*10*, *25*). It may be possible that by further optimizing contact and reducing channel length to the $L \sim 20$ nm region (*25*), higher on-current near-ballistic graphene FETs could be obtained. Assessment of carrier mobility requires more accurate gate capacitances (*26*, *27*) than are currently available. Analysis based on electrostatic simulations of gate capacitances led to an estimated hole mobility in the $w \leq 10$ nm ribbons of ~100 to 200 cm^2/V s. This high mobility suggests that the GNRs are of high quality, nearly pristine, and free of excessive covalent functionalization, which is consistent with spectroscopic data [fig. S2 (*18*)]. More precise mobility analysis will require accurate data on gate capacitances, GNR width and edge structures (*28*), and ensuring ohmic contacts to the ribbons. At the present time, the experimentally observed all-semiconducting nature of narrow GNRs appears to be a key advantage over SWNTs as candidates for future nanoelectronics.

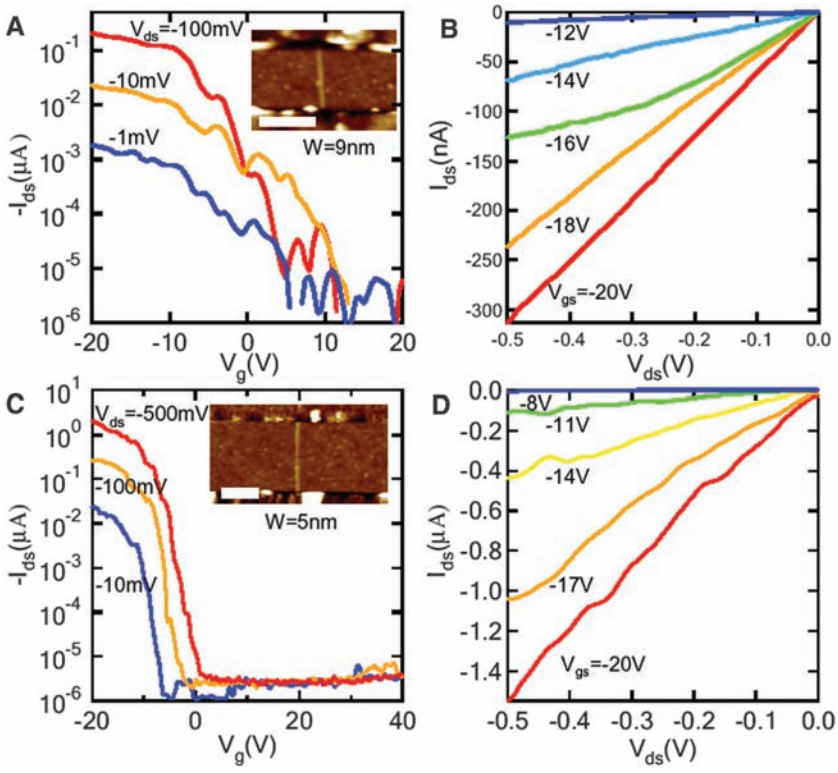

Fig. 3. Room-temperature graphene nanoribbon FETs with high on-off ratios. (**A**) Transfer characteristics (current versus gate voltage I_{ds}-V_{gs}) for a $w \approx 9$ nm (thickness ~ 1.5 nm, ~two layers) and channel length L ~ 130 nm GNR with Pd contacts and Si backgate. (Inset) AFM image of this device. Scale bar is 100 nm. (**B**) Current-voltage (I_{ds}-V_{ds}) curves recorded under various V_{gs} for the device in (A). (**C**) Transfer characteristics for a $w \approx 5$ nm (thickness ~ 1.5 nm, ~two layers) and channel length L ~ 210 nm GNR with Pd contacts. (Inset) The AFM image of this device. Scale bar is 100 nm. (**D**) I_{ds}-V_{ds} characteristics recorded under various V_{gs} for the device in (C).

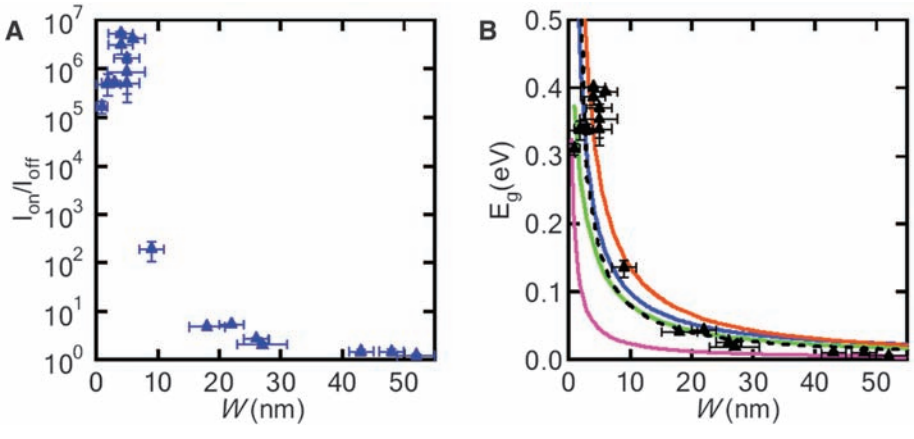

Fig. 4. Electrical properties of graphene nanoribbon FETs. (**A**) I_{on}/I_{off} ratios (under $V_{ds} = 0.5$ V) for GNRs of various ribbon widths measured in this work. Error bars for the x axis have their bases in uncertainties in ribbon width based from AFM measurements. Error bars for the y axis have their bases in the fluctuations in off state current (as shown in Fig. 3). (**B**) E_g extracted from experimental data (symbols) for various GNRs versus ribbon width. The black dashed line is a fit of our experimental data into an empirical form of E_g(eV) = 0.8/[w(nm)]. The purple, blue, and orange solid lines are first-principle calculations [Eqs. 1, 2, and 3 in (*18*)] for three types of armchair-edged GNRs respectively, and the green solid line is calculations for zigzag-edged GNRs [Eq. 4 of (*18*)], all based on (*7*).

References and Notes

1. A. K. Geim, K. S. Novoselov, *Nat. Mater.* **6**, 183 (2007).
2. K. S. Novoselov *et al.*, *Science* **306**, 666 (2004).
3. K. S. Novoselov *et al.*, *Nature* **438**, 197 (2005).
4. Y. B. Zhang, Y. W. Tan, H. L. Stormer, P. Kim, *Nature* **438**, 201 (2005).
5. C. Berger *et al.*, *Science* **312**, 1191 (2006); published online 12 April 2006 (10.1126/science.1125925).
6. C. Berger *et al.*, *J. Phys. Chem. B* **108**, 19912 (2004).
7. Y.-W. Son, M. L. Cohen, S. G. Louie, *Phys. Rev. Lett.* **97**, 216803 (2006).
8. V. Barone, O. Hod, G. E. Scuseria, *Nano Lett.* **6**, 2748 (2006).
9. D. A. Areshkin, D. Gunlycke, C. T. White, *Nano Lett.* **7**, 204 (2007).
10. G. C. Liang, N. Neophytou, D. E. Nikonov, M. S. Lundstrom, *IEEE Trans. Electron. Dev.* **54**, 677 (2007).
11. K. Nakada, M. Fujita, G. Dresslhaus, M. S. Dresselhaus, *Phys. Rev. B* **54**, 17954 (1996).
12. M. Y. Han, B. Ozyilmaz, Y. B. Zhang, P. Kim, *Phys. Rev. Lett.* **98**, 206805 (2007).
13. Z. Chen, Y. M. Lin, M. J. Rooks, P. Avouris, http://arxiv.org/abs/cond-mat/0701599 (2007).
14. S. Stankovich, R. D. Piner, S. T. Nguyen, R. S. Ruoff, *Carbon* **44**, 3342 (2006).
15. H. C. Schniepp *et al.*, *J. Phys. Chem. B* **110**, 8535 (2006).
16. A. P. Yu, P. Ramesh, M. E. Itkis, E. Bekyarova, R. C. Haddon, *J. Phys. Chem. C* **111**, 7565 (2007).

17. E. Rollings *et al.*, *J. Phys. Chem. Solids* **67**, 2172 (2006).
18. Materials and methods are available on *Science* Online.
19. H. Boehm, R. Setton, E. Stumpp, *Pure Appl. Chem.* **66**, 1893 (1994).
20. R. A. Greinke *et al.*, U.S. Patent 6,416,815.
21. A. D. Lueking, L. Pan, D. L. Narayanan, C. E. B. Clifford, *J. Phys. Chem. B* **109**, 12710 (2005).
22. A. Star *et al.*, *Angew. Chem. Int. Ed.* **40**, 1721 (2001).
23. X. L. Li *et al.*, *J. Am. Chem. Soc.* **129**, 4890 (2007).
24. A. Javey, J. Guo, Q. Wang, M. Lundstrom, H. Dai, *Nature* **424**, 654 (2003).
25. Y. Ouyang, Y. Yoon, J. Guo, *IEEE Trans. Electron. Dev.* **54**, 2223 (2007).
26. S. Ilani, L. A. K. Donev, M. Kindermann, P. L. McEuen, *Nat. Phys.* **2**, 687 (2006).
27. R. Tu, L. Zhang, Y. Nishi, H. Dai, *Nano Lett.* **7**, 1561 (2007).
28. Y. Yoon, J. Guo, *Appl. Phys. Lett.* **91**, 073103 (2007).
29. We thank Graftech for providing the samples. This work was supported by Microelectronics Advanced Research Corporation Materials, Structures, and Devices Focus Center (MARCO MSD) and Intel.

Supporting Online Material
www.sciencemag.org/cgi/content/full/1150878/DC1
Materials and Methods
Figs. S1 to S7
References

24 September 2007; accepted 10 January 2008
Published online 24 January 2008;
10.1126/science.1150878
Include this information when citing this paper.

Deeply Inverted Electron-Hole Recombination in a Luminescent Antibody-Stilbene Complex

Erik W. Debler,[1,2]* Gunnar F. Kaufmann,[2,3,4] Michael M. Meijler,[2,3]† Andreas Heine,[1]‡ Jenny M. Mee,[2,3] Goran Pljevaljčić,[1] Angel J. Di Bilio,[5] Peter G. Schultz,[2,3] David P. Millar,[1] Kim D. Janda,[2,3,4,6] Ian A. Wilson,[1,2] Harry B. Gray,[5]§ Richard A. Lerner[1,2,3]§

The blue-emissive antibody EP2-19G2 that has been elicited against *trans*-stilbene has unprecedented ability to produce bright luminescence and has been used as a biosensor in various applications. We show that the prolonged luminescence is not stilbene fluorescence. Instead, the emissive species is a charge-transfer excited complex of an anionic stilbene and a cationic, parallel π-stacked tryptophan. Upon charge recombination, this complex generates exceptionally bright blue light. Complex formation is enabled by a deeply penetrating ligand-binding pocket, which in turn results from a noncanonical interface between the two variable domains of the antibody.

An excited-state complex (exciplex) formed by the interaction of an electronically excited molecule with a ground-state partner features charge transfer to a various extent and typically exhibits structureless emission that is red-shifted from the emissive features of its individual components (*1*, *2*). Among the rare examples of exciplex-like behavior in proteins (*3*) is the conjugate of monoclonal antibody EP2-19G2 with the *trans*-stilbene hapten **1** (Scheme 1), which emits intense blue light upon ultraviolet (UV) excitation (movie S1) (*4*).

In striking contrast to this highly luminescent complex, electronically excited *trans*-stilbene is only weakly fluorescent in solution, owing to efficient nonradiative decay via cis-trans isomerization (*5*). Unlike other antibody-stilbene complexes (*4*, *6*), the radiative lifetime of EP2-19G2-**1** is increased by more than two orders of magnitude with respect to free **1**, which substantially exceeds those of stilbene exciplexes formed with small organic molecules (*7*). From extensive examination of the structures and photophysical properties of several antibody-**1** conjugates, we have concluded that the bright blue-emissive species is a tryptophan:stilbene charge-transfer excited complex that undergoes deeply inverted electron-hole recombination in a rigid protein matrix.

Guided by the crystal structure of EP2-19G2-**1** (*4*), we identified seven antibody residues in van der Waals' contact with the stilbene aromatic system. These seven residues were then conservatively mutated and the corresponding proteins were expressed as single-chain variable antibody fragments (scFv) (*8*, *9*). Spectroscopic measurements indicated that mutation of Trp^{H103} to Phe ($Trp^{H103}Phe$) and Tyr^{L34} to Phe ($Tyr^{L34}Phe$) markedly reduced antibody-**1** emissions when compared to scFv wild-type (wt)-**1** [Fig. 1B and fig. S1 (*9*)]. As observed in the crystal structure of the EP2-19G2-**1** complex, the indole ring of Trp^{H103} is π-stacked parallel to the deeply buried phenyl ring of the stilbene ligand at an inter-

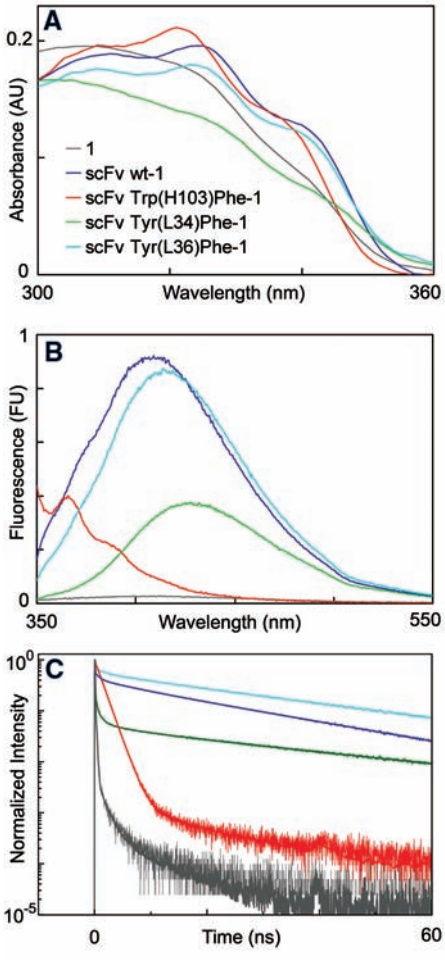

Fig. 1. (**A**) Steady-state absorption spectra of **1** (10 μM) and antibody-**1** complexes (10 μM) in PBS containing 3% DMF at room temperature. (**B**) Steady-state emission spectra of **1** (20 nM) and antibody-**1** complexes (20 nM) in PBS containing 3% DMF at room temperature. Antibody was used in large excess to ensure that the dye was completely bound by protein. (**C**) Time-resolved emission decay profiles of antibody-**1** complexes (3 μM) obtained with picosecond excitation at 303 nm. Decays were measured by time-correlated single-photon counting. Decays were recorded in 4096 channels with a time increment of 22 ps/channel and were normalized relative to the number of counts recorded in the peak channel.

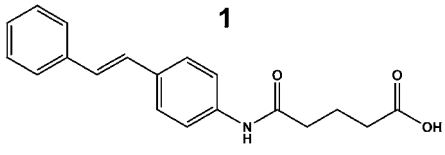

Scheme 1.

[1]Department of Molecular Biology, The Scripps Research Institute, La Jolla, CA 92037, USA. [2]The Skaggs Institute for Chemical Biology, The Scripps Research Institute, La Jolla, CA 92037, USA. [3]Department of Chemistry, The Scripps Research Institute, La Jolla, CA 92037, USA. [4]Department of Immunology, The Scripps Research Institute, La Jolla, CA 92037, USA. [5]Beckman Institute, California Institute of Technology, Pasadena, CA 91125, USA. [6]Worm Institute of Research and Medicine, The Scripps Research Institute, La Jolla, CA 92037, USA.

*Present address: Laboratory of Cell Biology, The Rockefeller University, New York, NY 10065, USA.
†Present address: Department of Chemistry, Ben-Gurion University of the Negev, Israel.
‡Present address: Institute of Pharmaceutical Chemistry, Philipps-University Marburg, 35032 Marburg, Germany.
§To whom correspondence should be addressed. E-mail: rlerner@scripps.edu (R.A.L.); hbgray@caltech.edu (H.B.G.)